Fuel 416 (2026) 138533

Contents lists available at ScienceDirect

Fuel

journal homepage: www.elsevier.com/locate/fuel

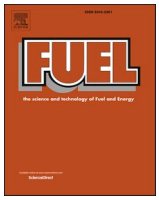

Full Length Article

Efficient Oxygen Evolution Using Conductive Nitrogen-rich Ferrocene-based Porous Organic Polymers Electrocatalysts

Ahmed F. Saber [a], Mohamed Gamal Mohamed [b,*], Munzir H. Suliman [a], Shiao-Wei Kuo [b], Mahmoud M. Abdelnaby [a,*]

[a] Interdisciplinary Research Center for Hydrogen Technologies and Carbon Management (IRC-HTCM), King Fahd University of Petroleum & Minerals, Dhahran 31261, Saudi Arabia
[b] Department of Materials and Optoelectronic Science, National Sun Yat-Sen University, Kaohsiung 80424, Taiwan

ARTICLE INFO

Keywords:
Porous Organic Polymers (POPs)
Ferrocene
Triazine
Schiff-base condensation
Electrocatalysis
Oxygen Evolution

ABSTRACT

The development of stable, efficient, and cost-effective electrocatalysts for the oxygen evolution reaction (OER) is critically important due to the intrinsically sluggish kinetics of this process, which significantly limit the efficiency of water splitting and related electrochemical energy systems. Porous organic polymers (POPs) have recently emerged as a versatile platform for the design of heterogeneous catalysts; however, their application in water-splitting electrocatalysis, particularly for the OER, remains largely unexplored. In this work, two novel ferrocene-based porous POP electrodes were designed, synthesized, and subsequently supported on nickel foam (NF) for evaluation as OER electrocatalysts. The resulting electrodes exhibit remarkable electrocatalytic activity and excellent operational stability under alkaline OER conditions. Notably, in 1.0 M KOH, the most active catalyst, Fc-PBTD POP, achieves a low overpotential of approximately 291 mV at a current density of 10 mA cm^{-2}, along with a small Tafel slope of 86 mV dec^{-1}. Furthermore, the catalyst demonstrates outstanding durability, retaining its activity with negligible performance degradation over 15 h of continuous chronoamperometric operation. Electrochemical analyses reveal that the superior OER performance originates from the incorporation of ferrocene units, which act as efficient electron-transfer mediators, facilitating rapid charge transport and enhancing overall catalytic activity. This study represents a significant advancement in the design of ferrocene-functionalized porous POP electrocatalysts and contributes new insights into their potential for energy-related electrocatalytic applications.

1. Introduction

The increasing dependence on fossil fuel resources has led to severe environmental pollution, driving the urgent need for cleaner and renewable energy alternatives to meet global energy demands in a sustainable manner [1–3]. In recent decades, electrochemical water splitting has emerged as a key technology for sustainable energy conversion, providing a clean and efficient route for hydrogen production from water [4]. This process involves two half-reactions: the hydrogen evolution reaction (HER) at the cathode and the oxygen evolution reaction (OER) at the anode, both of which critically influence the overall efficiency of water splitting [5]. Among them, the OER is widely recognized as the rate-limiting step due to its intrinsically sluggish kinetics compared with the HER, thereby representing a major bottleneck in improving system performance [6,7]. Consequently, the development of highly efficient OER electrocatalysts is essential for advancing not only water-splitting technologies [8] but also related energy-conversion systems such as fuel cells [9] and metal–air batteries, where oxygen evolution strongly affects device efficiency and durability [10].

Noble metal oxides, including RuO_2 and IrO_2, are benchmark OER catalysts owing to their outstanding catalytic activity [11,12]. However, their high cost and limited natural abundance severely hinder large-scale industrial deployment, necessitating the exploration of more economical and sustainable alternatives [13,14]. In this context, a variety of earth-abundant transition metal-based materials—such as oxides [15], carbides [16,17], phosphides [18,19], nitrides [20,21], and chalcogenides [22,23] have been extensively investigated as potential OER electrocatalysts. Although these materials often exhibit promising catalytic activity, many still suffer from critical drawbacks, including insufficient long-term stability, limited selectivity, and vulnerability to

* Corresponding authors.
E-mail addresses: mgaml.eldin12@aun.edu.eg (M.G. Mohamed), mahmoudm@kfupm.edu.sa (M.M. Abdelnaby).

https://doi.org/10.1016/j.fuel.2026.138533
Received 11 November 2025; Received in revised form 18 January 2026; Accepted 24 January 2026
Available online 29 January 2026

surface poisoning, which impede their practical application in OER and other electrochemical systems [24]. As a result, increasing attention has been directed toward the design of stable transition metal-based catalysts integrated within large organic frameworks featuring low metal loading and abundant electrochemically active sites. Such hybrid architectures are expected to enhance durability, selectivity, and resistance to deactivation, offering a more sustainable and efficient strategy for OER catalysis [25,26].

Recent reviews have highlighted the persistent challenges and emerging strategies in advancing electrocatalytic water splitting, particularly at the OER half-cell. Zhang et al. provided a comprehensive overview of asymmetric catalyst design strategies, with a focus on non-precious metal systems for water electrolysis and related energy-conversion technologies, emphasizing the inherent trade-offs among catalytic activity, stability, and scalability [27]. In addition to activity optimization, long-term durability has been identified as a critical consideration in catalyst design. Recent studies have systematically summarized the key factors governing OER stability, including morphological evolution, phase transformation, and catalyst dissolution, as well as effective mitigation strategies such as structural regulation and protective surface coatings [28]. These reviews underscore the need for catalysts that combine high activity with structural robustness, which exhibit both low overpotential and strong stability under OER conditions.

Porous organic polymers (POPs) are multidimensional porous frameworks constructed from diverse organic building blocks with various topologies and geometries, interconnected through strong covalent bonds. This structural versatility endows POPs with high thermal and chemical stability, along with tunable porosity suitable for a wide range of applications [29,30]. Based on the degree of long-range structural order, POPs can be broadly classified into amorphous POPs, which lack long-range periodicity—such as porous aromatic frameworks (PAFs), conjugated microporous polymers (CMPs), and hypercrosslinked polymers (HCPs)—and crystalline POPs, which exhibit well-defined periodic structures, most notably covalent organic frameworks (COFs) [31–45]. Owing to their high surface areas, tunable architectures, abundant exposed active sites, and adjustable pore sizes, POPs have attracted increasing attention in electrocatalysis. Moreover, the wide selection of organic building blocks allows facile incorporation of heteroatoms and metal species into the porous frameworks, enabling the rational design of catalysts with enhanced activity, selectivity, and stability [46,47]. To date, only a limited number of studies have explored POPs as electrocatalysts for OER. For example, Yang's research group synthesized a phenazine-linked COF [48], Mondal's group developed a thiadiazole-based COF [49], and Das's team reported a POP incorporating pyrene and benzothiadiazole units [50], all of which demonstrated promising OER activity. In addition, metal doping has been widely employed to further improve the electrocatalytic performance of POPs, as incorporated metal species can enhance electrical conductivity, increase active-site density, and facilitate electron-transfer processes [51]. all of which demonstrated promising OER activity. In addition, metal doping has been widely employed to further improve the electrocatalytic performance of POPs, as incorporated metal species can enhance electrical conductivity, increase active-site density, and facilitate electron-transfer processes.

Ferrocene (Fc) is a prototypical "sandwich-type" organometallic complex renowned for its unique redox properties and chemical stability. Its exceptional redox behavior arises from the aromatic nature of the two cyclopentadienyl rings symmetrically coordinated to the central iron atom, which enables efficient electron delocalization and highly reversible Fe(II)/Fe(III) redox transitions. Recent studies have shown that incorporating Fc motifs into porous frameworks, such as metal–organic frameworks (MOFs) and COFs, can significantly enhance OER activity by improving electron-transfer pathways and enabling redox mediation. For instance, a cobalt–ferrocene MOF constructed using 1,1′-ferrocenedicarboxylic acid (FcDA) has been reported to undergo structural reconstruction under OER conditions, highlighting the role of Fc-containing frameworks as effective precatalysts [52]. Similarly, immobilization of Fc derivatives within MOF hosts, such as ZIF-8, has demonstrated competitive OER performance, further supporting the ability of Fc units to modulate catalytic behavior [53]. In addition, Budnikova and co-workers reported the use of Fc-based compounds as catalysts for HER, employing Fc diphosphonate and 4,4′-bipyridine ligands in MOF synthesis [54]. Edmund's group also explored Fc-containing compounds as OER precatalysts, where nickel species were shown to play a crucial role in enhancing electrocatalytic activity [55]. Together with broader electrocatalyst design principles summarized in recent reviews [27]. These studies motivate the development of Fc-functionalized POPs for OER applications. Although several pioneering works have investigated Fc-based materials as electrocatalysts, their utilization in OER remains relatively underexplored. The distinctive molecular structure of Fc, characterized by its stable and redox-active sandwich configuration, therefore offers significant yet underutilized potential for advancing OER electrocatalysis.

Motivated by the excellent electronic properties of the Fc moiety, we successfully designed and synthesized two POPs via a straightforward and efficient condensation reaction between Fc-2$COCH_3$ and either melamine or PBTD-4NH_2, targeting their application in OER (Scheme 1). The incorporation of nitrogen-rich, electron-deficient triazine units with robust C=N linkages, together with the Fe center and unique redox characteristics of the Fc moiety, provides a versatile platform for heterogeneous catalysis. This synergistic structural and electronic integration enhances both framework stability and charge transport, making the resulting polymers particularly suitable for OER electrocatalysis. Notably, extended π–π stacking interactions between the aromatic Fc units along the polymer backbone promote the formation of nanosheet-like morphologies with high surface area, which significantly improve catalytic performance by increasing the exposure of electroactive sites and facilitating efficient electron transfer throughout the material. Benefiting from their high surface area and improved electrical conductivity, the as-synthesized polymers exhibit excellent OER activity, achieving a low overpotential of 291 mV at a current density of 10 mA cm^{-2} (vs. RHE) in alkaline electrolyte. This performance is comparable to that of commercial OER catalysts, highlighting the strong potential of these materials for practical electrochemical energy-conversion applications. Overall, this work provides valuable insights into the rational design of N-rich, Fc-functionalized polymeric catalysts, offering a promising strategy for developing efficient and sustainable electrocatalysts for OER and related energy applications.

2. Experimental section

2.1. Materials

Ferrocene (Fc), aluminum chloride ($AlCl_3$), acetyl chloride (AcCl), melamine (Mel), dichloromethane (DCM), chloroform ($CHCl_3$), 2-cyanoguanidine, potassium hydroxide (KOH), dimethyl formamide (DMF), dimethyl sulphoxide (DMSO), 1,4-dicyanobenzene, tetrahydrofuran (THF), acetone, ethanol (EtOH) and methanol (MeOH) were gained from different trade resources, including Sigma-Aldrich (Louis, USA), Acros (New Jersey, USA), and Alfa-Aesar (Lancashire, UK).

2.2. Synthesis of Fc-Mel POP

Fc-2Ac (0.44 g, 1.42 mmol) and Mel-3NH_2 (0.14 g, 1.11 mmol) have been added to a round-bottomed flask and refluxed at 180 °C in 50 mL of DMSO under N_2 atmosphere for 72 h. After completion of the reaction, the mixture was allowed to cool to room temperature, yielding a black precipitate that was collected by filtration and subsequently purified by Soxhlet extraction using THF, $CHCl_3$, MeOH, and acetone. Finally, the black polymer obtained was dried at 110 °C for 24 h (Scheme S3). FTIR (KBr, cm^{-1}, Fig. S5): 3128 (C–H aromatic), 2920 (C–H aliphatic), 1637

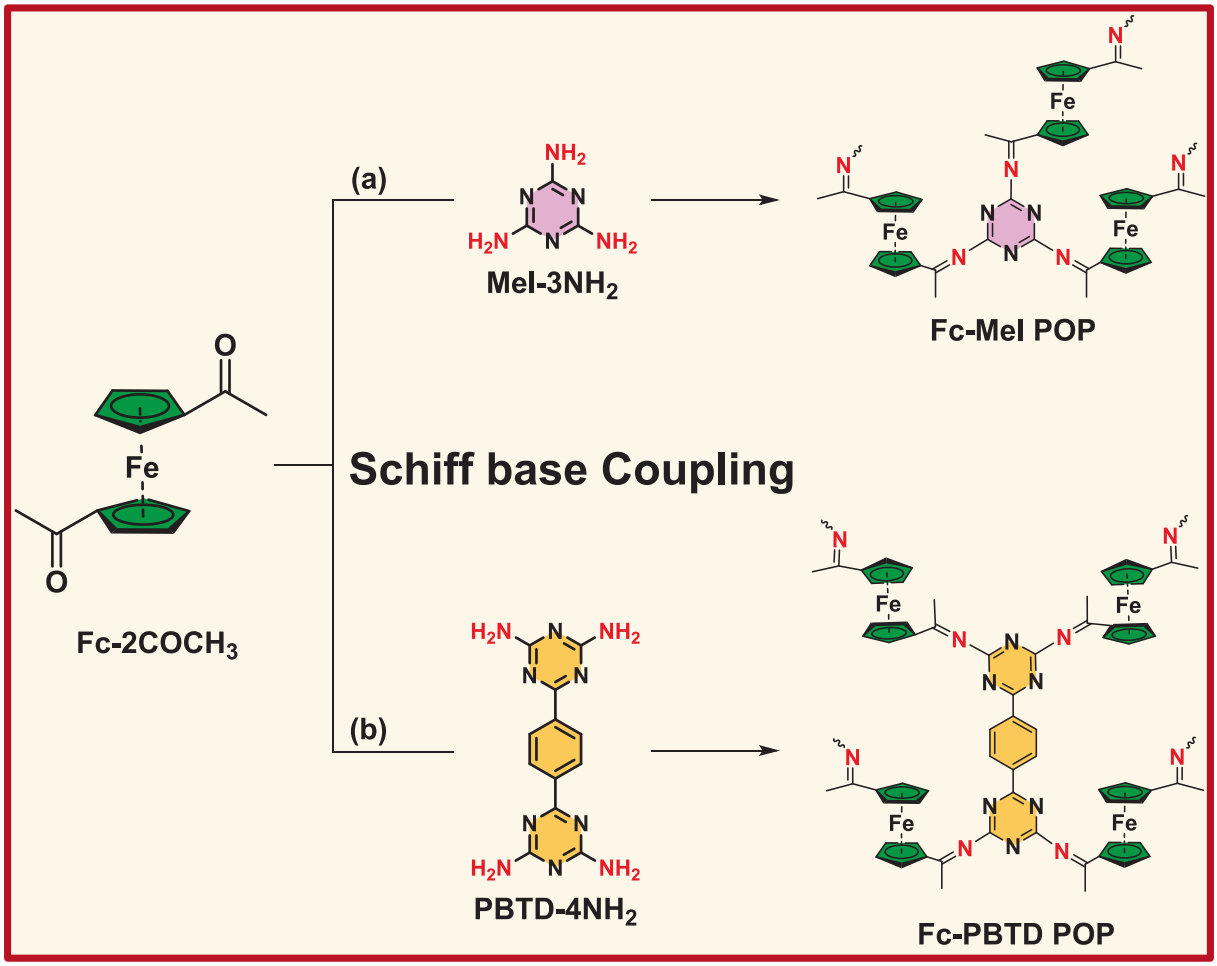

Scheme 1. Synthesis of the Fc-Mel and Fc-PBTD POPs.

(C=N), 1371, 1200 (C–N), 1032 (C=C of Fc).

2.3. Synthesis of Fc-PBTD POP

Fc-2Ac (0.44 g, 1.42 mmol) and PBTD-4NH_2 (0.24 g, 0.81 mmol) have been added to a round-bottomed flask and refluxed at 180 °C in 50 mL of DMSO under N_2 atmosphere for 72 h. After completion of the reaction, the mixture was allowed to cool to room temperature, yielding a black precipitate that was collected by filtration and subsequently purified by Soxhlet extraction using THF, $CHCl_3$, MeOH, and acetone. Finally, the obtained black polymer was dried at 110 °C for 24 h (Scheme S4). FTIR (KBr, cm^{-1}, Fig. S6): 3049 (C–H aromatic), 2923 (C–H stretching), 1653 (C=N), 1371, 1204 (C–N), 1044 (C=C of Fc).

2.4. Electrochemical measurements

The working electrode was fabricated by drop-casting catalyst ink onto a nickel foam (NF) with an area of 1.0 cm^2. The catalyst ink was prepared by adding 2 mg of the prepared sample and 1 mg of carbon black to a solution containing 400 μL of ethanol, 380 μL of deionized water, and 20 μL of Nafion. The mixture was sonicated for 45 min to make a homogeneous catalyst ink. To prepare the working electrode, 10 μL of the catalyst ink was drop-casted onto NF and dried in an oven at 70 °C for 15 min. The electrochemical tests were carried out in a typical three-electrode system connected to a computer-controlled potentiostat INTERFACE 1010 E at room temperature. Platinum wire was used as a counter electrode. Ag/AgCl was utilized as a reference electrode for alkaline electrolytes. The polarization curve of OER was obtained in 1.0 M KOH electrolyte at a scan rate of 100 mV s^{-1} for all samples. All potentials are converted to reversible hydrogen electrodes (RHE) based on the Nernst equation:

$$E_{RHE} = E_{Ag/AgCl} + E^{0}_{Ag/AgCl} + 0.059\ pH.$$

The EIS spectra were recorded in the frequency range of 1 Hz to 100 kHz by applying an amplitude of 5 mV at 280 mV versus RHE.

The overpotential (η) can be estimated from the following equation:

$$\eta = E_{RHE} - 1.23.$$

The Tafel slope can be estimated from the LSV curve using the following relationship:

$$\eta = b \log j + a.$$

in which "b" refers to the Tafel slope and the term "a" is a constant.

3. Results and discussion

3.1. Structural design, preparation, and characterization

The N-rich composition, degree of π-conjugation, and incorporation of metal centers in the building monomers play a decisive role in determining the electrocatalytic OER performance of POPs. Nitrogen atoms enhance intrinsic electronic conductivity through electron-donating effects and provide active coordination sites that facilitate charge transfer and stabilize reaction intermediates. Meanwhile, a higher degree of π-conjugation promotes efficient electron delocalization along the polymer backbone, thereby improving charge mobility and redox activity. Collectively, these structural features synergistically enhance catalytic efficiency, reduce the overpotential, and improve the long-term stability of POP-based OER electrocatalysts.

Based on these considerations, N-rich Fc-based POPs, namely Fc-Mel POP and Fc-PBTD POP, were synthesized via a Schiff-base condensation reaction between 1,1′-diacetylferrocene (Fc-2Ac) and the monomers Mel-3NH_2 or PBTD-4NH_2, respectively, in DMSO at 180 °C under a nitrogen atmosphere (Schemes S3 and S4). The resulting polymers (Scheme 1) were characterized using Fourier transform infrared spectroscopy (FTIR), solid-state ^{13}C nuclear magnetic resonance (SS ^{13}C NMR), and X-ray photoelectron spectroscopy (XPS).

Successful polymerization was first confirmed by FTIR and SS ^{13}C NMR analyses. As shown in Fig. 1a, Fc-Mel POP and Fc-PBTD POP exhibit characteristic absorption bands at 1023 and 1044 cm^{-1}, respectively, corresponding to the C=C stretching vibrations of the Fc unit. In addition, Fc-Mel POP displays absorption bands at approximately 1632 and 1371 cm^{-1}, assigned to C=N and C–N stretching vibrations, respectively, while the corresponding peaks for Fc-PBTD POP appear at 1653 and 1371 cm^{-1}. Furthermore, absorption bands at 2920 and 2923 cm^{-1}, attributed to aliphatic C–H stretching vibrations from the acetyl groups of Fc, are observed for Fc-Mel and Fc-PBTD POPs, respectively.

The SS ^{13}C NMR spectra (Fig. 1b) further support the successful formation of the polymer frameworks. Fc-Mel POP exhibits signals in the range of 76–89 ppm, assigned to Fc carbons, while Fc-PBTD POP shows corresponding signals between 73 and 92 ppm. Broad resonances in the 114–142 ppm region for Fc-PBTD POP are attributed to aromatic carbons. Signals at 165 and 166 ppm correspond to triazine carbons in Fc-Mel and Fc-PBTD POPs, respectively, whereas additional peaks at 184 and 178 ppm are assigned to the C=N carbons of the Schiff-base linkages.

Thermal stability was evaluated by thermogravimetric analysis (TGA) under a nitrogen atmosphere. Both polymers exhibit high thermal stability, with Fc-PBTD POP displaying a slightly higher decomposition temperature (291 °C) compared to Fc-Mel POP (258 °C). The char yields of Fc-Mel and Fc-PBTD POPs were determined to be 51% and 50%, respectively (Fig. S7 and Table S1), confirming the robust nature of the polymer frameworks.

X-ray photoelectron spectroscopy (XPS) was employed to investigate the surface chemical composition and bonding environments of Fc-Mel POP and Fc-PBTD POP. Survey spectrum confirms the presence of C, N, and Fe, consistent with the proposed Schiff's base polymer structures (Fig. S8). In the high-resolution C 1s spectra, dominant peaks at approximately 283.9 and 284.4 eV are attributed to C–C/C=C bonds from the aromatic backbone and Fc units in Fc-Mel and Fc-PBTD POPs, respectively. Peaks at higher binding energies (~286.0–286.4 eV) correspond to C–N and C=N species, confirming the formation of imine linkages. The N 1s spectrum of Fc-Mel POP can be deconvoluted into components assigned to triazine C=N (~398.7 eV), triazine C–N (~399.9 eV), and Schiff-base C=N (~400.9 eV). Similarly, Fc-PBTD POP exhibits N 1s peaks at 397.8, 398.8, and 399.6 eV, corresponding to triazine C=N, triazine C–N, and Schiff's base C=N, respectively (Fig. 2). The high-resolution Fe 2p spectra provide insight into the oxidation state and local chemical environment of Fe centers within the polymers (Fig. 2c and 2f). For Fc-Mel POP, Fe $2p_{3/2}$ and Fe $2p_{1/2}$ peaks at approximately 709.3 and 722.8 eV are assigned to Fe(II) species originating from the ferrocene units. Weak satellite features at higher binding energies (~717.2 and 731.8 eV) are characteristic of shake-up processes associated with oxidized iron species, confirming the non-metallic nature of the Fe centers. Importantly, no Fe(0)-related peaks are observed, indicating that the Fc units remain chemically bound within the polymer framework.

In comparison, Fc-PBTD POP exhibits a similar Fe 2p doublet but with a noticeable shift toward higher binding energies and an increased contribution from Fe(III) species. Deconvolution reveals Fe(III) $2p_{3/2}$ and $2p_{1/2}$ peaks at approximately 711.8 and 725.5 eV, along with Fe(II)-related components and pronounced satellite features around 717 and 730.3 eV. This higher Fe(III) contribution suggests stronger electronic interactions between the Fc units and the more conjugated, N-rich PBTD linker, facilitating partial oxidation of Fe centers and enhancing redox-mediated electrocatalytic activity [56].

Notably, no FeOx-related features or broad multiplet structures characteristic of iron oxide phases are detected for either polymer, indicating that the Fe centers remain atomically dispersed and chemically stable within the polymer matrix. The higher Fe(III)/Fe(II) ratio observed for Fc-PBTD POP correlates well with its superior OER performance [52]. Overall, Fe 2p XPS analysis confirms the successful incorporation of Fc moieties and highlights the critical role of the PBTD linker in tuning the electronic structure of the Fe active sites.

X-ray diffraction (XRD) patterns of Fc-Mel POP and Fc-PBTD POP (Fig. S9) are dominated by broad diffraction features, confirming their largely amorphous nature, which is typical for POPs [57–59]. Fc-PBTD POP shows a broad hump in the 20–30° (2θ) region, indicative of short-range ordering and π–π stacking within the conjugated framework, whereas Fc-Mel POP exhibits additional weak reflections (e.g., near ~ 30° and ~ 35°), suggesting the presence of minor crystalline impurities. These weak peaks are attributed to residual unreacted species or small crystallites formed during synthesis, rather than the polymer framework itself.

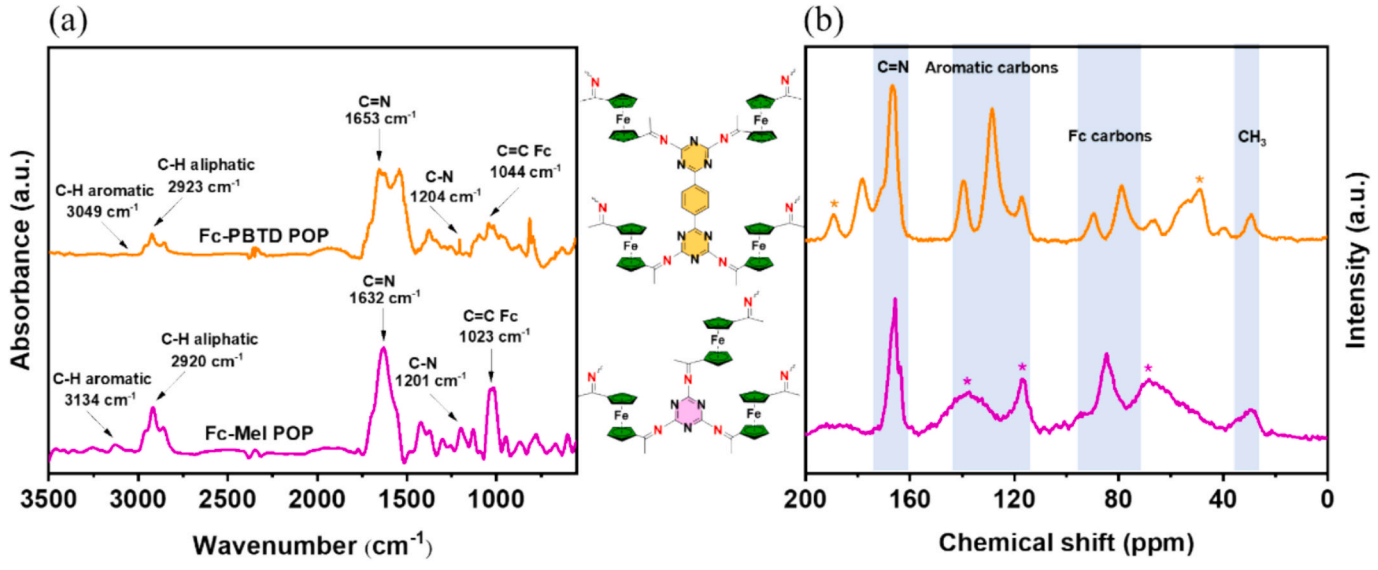

Fig. 1. (a) FTIR spectra; and (b) solid-state ^{13}C NMR spectra of the Fc-Mel POP, and Fc-PBTD POP.

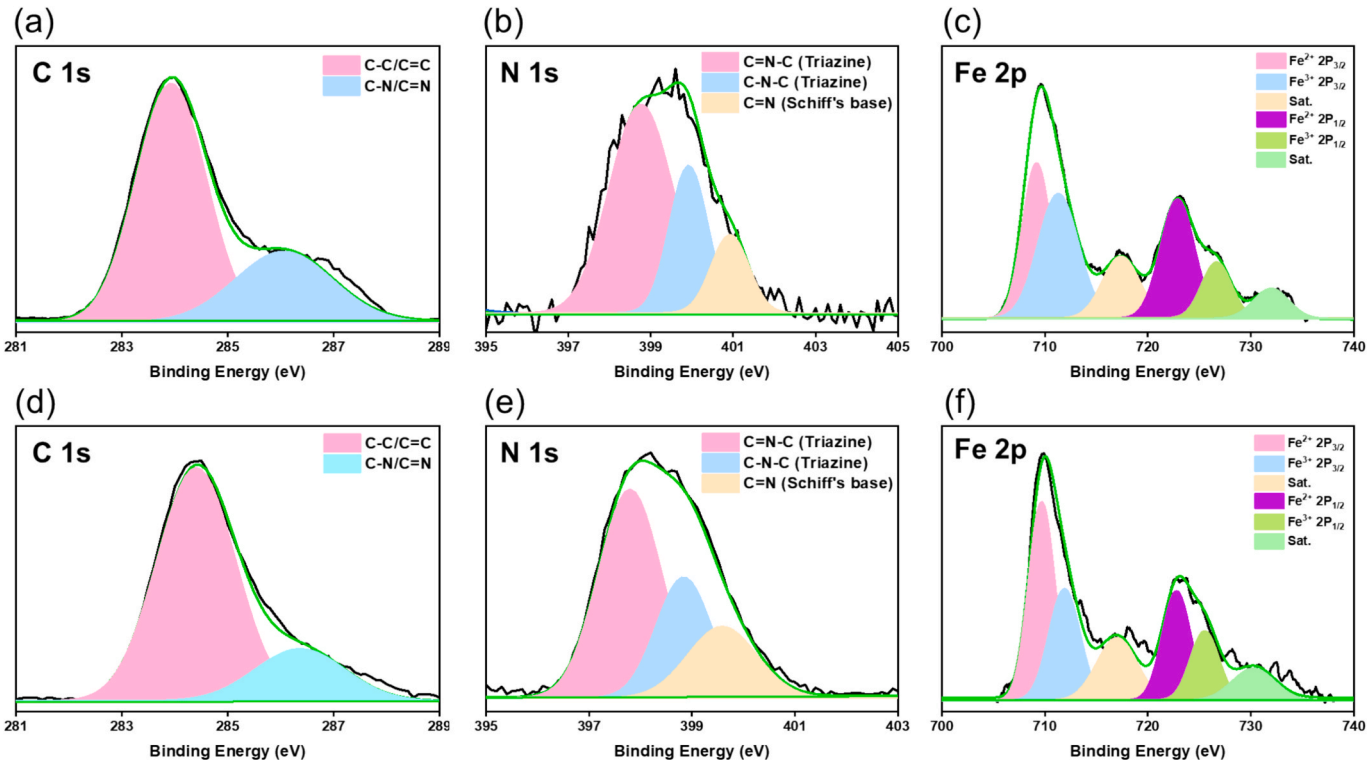

Fig. 2. XPS fitting of (a) C 1 s peak, (b) N 1 s, and (c) Fe 2p peak of Fc-Mel POP; (d) C 1 s peak, (e) N 1 s peak, and (f) Fe 2p peak of Fc-PBTD POP.

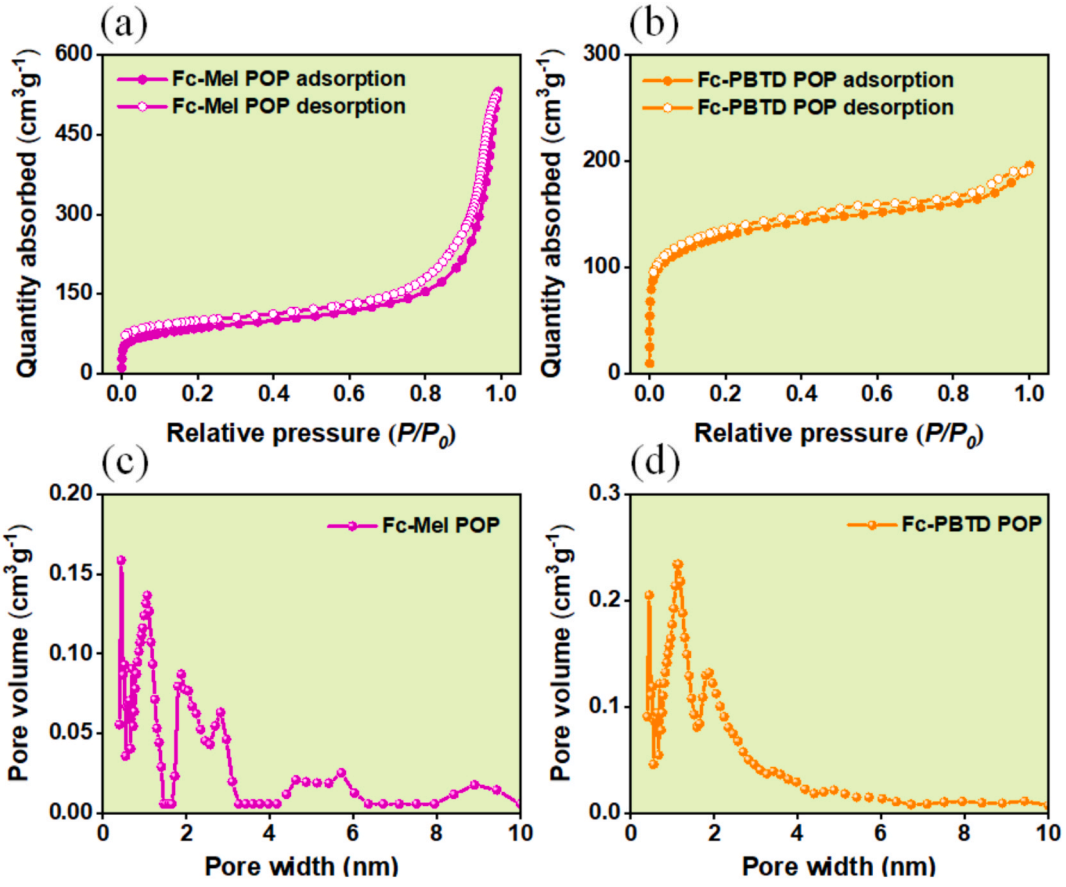

Fig. 3. N_2 adsorption–desorption isotherms of (a) Fc-Mel POP, and (b) Fc-PBTD POP; The corresponding pore size distribution curves of (c) Fc-Mel POP, and (d) Fc-PBTD POP.

Raman spectroscopy further elucidates differences in backbone conjugation and local ordering (Fig. S10). Both polymers display broad Raman features, consistent with their amorphous structures. Notably, Fc-PBTD POP exhibits stronger Raman intensities and more pronounced bands in the ~ 1000–1200 cm^{-1} and ~ 1500–1600 cm^{-1} regions, associated with aromatic ring and C–N/C=N stretching vibrations in conjugated N-containing frameworks. In contrast, Fc-Mel POP shows weaker and less defined bands, indicating a less extended π-conjugated network. These results suggest that the rigid and π-delocalized PBTD linker enhances electronic coupling between Fc units and the polymer backbone, improving charge transport and stabilizing redox-active sites during OER. Overall, the Raman analysis supports the formation of robust POP frameworks and further explains the superior OER activity and stability of Fc-PBTD POP.

3.2. Porosity and morphology

Nitrogen sorption measurements were performed at 77 K to evaluate the porosity of the synthesized polymers. Among the two materials, Fc-PBTD POP exhibits the highest Brunauer–Emmett–Teller (BET) surface area (S_{BET}) of 428 $m^2\ g^{-1}$, whereas Fc-Mel POP shows a lower S_{BET} of 293 $m^2\ g^{-1}$ (Fig. 3a and b). The pore size distributions were calculated using non-local density functional theory (NLDFT), revealing that both polymers are predominantly microporous in nature. Specifically, Fc-Mel POP displays a dominant pore width of 1.07 nm, while Fc-PBTD POP exhibits slightly larger micropores centered at 1.15 nm. Correspondingly, the total pore volumes were determined to be 0.14 $cm^3\ g^{-1}$ for Fc-Mel POP and 0.23 $cm^3\ g^{-1}$ for Fc-PBTD POP (Fig. 3c and d, Table 1).

Scanning electron microscopy (SEM) was employed to investigate the morphological differences between Fc-Mel POP and Fc-PBTD POP (Fig. S11). As shown in Figs. S11a and b, Fc-Mel POP exhibits an irregular and highly aggregated morphology composed of plate-like and fragmented particles with rough surfaces. At higher magnification (Fig. S11b), the material appears densely packed with non-uniform granules and agglomerates, indicating limited control over particle growth and reduced exposure of internal surfaces. Such compact aggregation may hinder electrolyte diffusion and restrict the accessibility of electroactive sites during electrocatalytic operation.

In contrast, Fc-PBTD POP shows a markedly different morphology (Figs. S11c and d). The polymer consists of more uniformly shaped, loosely packed particles with a relatively open and porous surface texture. High-magnification SEM images (Fig. S11d) reveal a well-distributed nanoscale granular structure with abundant surface protrusions, reflecting improved dispersion of polymer domains and increased surface roughness. This hierarchical morphology is advantageous for facilitating electrolyte penetration and maximizing the exposure of Fc active sites.

The pronounced morphological differences between the two polymers can be attributed to the distinct structural characteristics of their linkers. The rigid, extended, and π-conjugated PBTD linker promotes more homogeneous polymerization and suppresses excessive particle aggregation, resulting in a more open microstructure. In contrast, the smaller and more compact melamine linker favors denser packing and irregular particle growth. These morphological advantages of Fc-PBTD POP are consistent with its superior OER performance, as enhanced surface accessibility and improved mass transport are crucial for efficient electrocatalysis.

Transmission electron microscopy (TEM) was further used to examine the microstructural features of the polymers. TEM images confirm the microarchitectures of both materials and verify the successful incorporation of Fc units containing iron within the polymer frameworks (Fig. 4a and e), indicating preserved structural integrity. Energy-dispersive X-ray spectroscopy (EDS) elemental mapping reveals a homogeneous distribution of C, N, and Fe elements across the polymer surfaces (Fig. 4b–d and 4f–h), further supporting uniform metal incorporation throughout the frameworks.

Table 1
BET parameters of the as-synthesized POPs.

Material	S_{BET} ($m^2\ g^{-1}$)	Pore Size (nm)	Pore Volume ($cm^3\ g^{-1}$)
Fc-Mel POP	293	1.07	0.14
Fc-PBTD POP	428	1.15	0.23

3.3. Electrochemical oxygen evolution

The OER activity of the POP catalysts supported on nickel foam (POP@NF) was evaluated in 1.0 M KOH electrolyte. Initial cyclic voltammetry (CV) measurements were performed within a potential window of 0.0–1.0 V vs. RHE to probe the current–voltage behavior and electrochemical stability of the catalysts. These preliminary CV studies provide important insight into catalyst activation under operating conditions. Previous reports have shown that repeated CV cycling can promote the formation of highly oxidative electroactive species on catalyst surfaces, particularly for Ni-based systems, thereby enhancing OER kinetics and overall catalytic performance [60,61].

Ferrocene is known to undergo highly reversible Fe(II)/Fe(III) redox transitions with minimal energetic barriers, making it an effective electron-transfer mediator and a widely used electrochemical internal standard [62,63]. As shown in the CV profiles (Fig. S12), the Fc-PBTD POP@NF electrode exhibits a distinct anodic peak at approximately 0.46 V vs. RHE, followed by a sharp increase in catalytic current, which is attributed to the oxidation of Fe(II) to Fe(III). During the cathodic sweep, a broad reduction peak centered at approximately 0.35 V vs. RHE is observed, corresponding to the reduction of Fe(III) species to Fe(II). This reversible redox behavior is consistent with previous reports [64] and reflects the efficient redox activity of the Fc units, supporting their role in facilitating OER catalysis. The Fc-Mel POP@NF electrode also displays redox features, albeit with comparatively weaker activity, highlighting the superior electrocatalytic behavior of the Fc-PBTD POP.

Subsequently, linear sweep voltammetry (LSV) was conducted at a scan rate of 50 mV s^{-1} in 1.0 M KOH to assess the OER performance of pristine NF, Fc-Mel POP@NF, and Fc-PBTD POP@NF. As shown in Fig. 5a, Fc-PBTD POP@NF exhibits the most pronounced catalytic activity, with a notably lower onset potential of approximately 0.49 V vs. RHE, compared to 0.55 V vs. RHE for Fc-Mel POP@NF. A rapid increase in current density is observed, reaching ~ 340 mA cm^{-2}, indicative of fast electron-transfer kinetics. Such behavior is very favorable for OER applications, as it indicates a fast heterogeneous electron transportation process at the active surface sites of the electrocatalyst [65]. In contrast, pristine NF shows only a modest current response, confirming that the enhanced OER activity arises primarily from the POP catalyst layer rather than the substrate. To achieve a benchmark current density of 10 mA cm^{-2}, Fc-PBTD POP@NF requires a low overpotential of 291 mV, which is comparable to that of commercial RuO_2 (320 mV) [66]. Fc-Mel POP@NF, by comparison, requires a higher overpotential of ~ 359 mV, reflecting its lower catalytic efficiency.

At higher current densities of 25, 50, and 100 mA cm^{-2}, Fc-PBTD POP@NF consistently outperforms Fc-Mel POP@NF, requiring overpotentials of 336, 389, and 484 mV, respectively, whereas Fc-Mel POP@NF requires 398, 442, and 511 mV under identical conditions (Fig. 5b). These results clearly demonstrate the superior OER performance of the Fc-PBTD system.

Tafel analysis was performed to evaluate intrinsic reaction kinetics and charge-transfer characteristics. As shown in Fig. 5c, Fc-PBTD POP@NF exhibits a low Tafel slope of 86 mV dec^{-1}, significantly smaller than those of Fc-Mel POP@NF (110 mV dec^{-1}) and pristine NF (128 mV dec^{-1}), indicating faster OER kinetics. Notably, the Tafel slope of Fc-PBTD POP@NF is also lower than those reported for several polymer-based OER catalysts and even commercial RuO_2 (98 mV dec^{-1}), highlighting its competitive catalytic efficiency [66].

Electrochemical impedance spectroscopy (EIS) was employed to

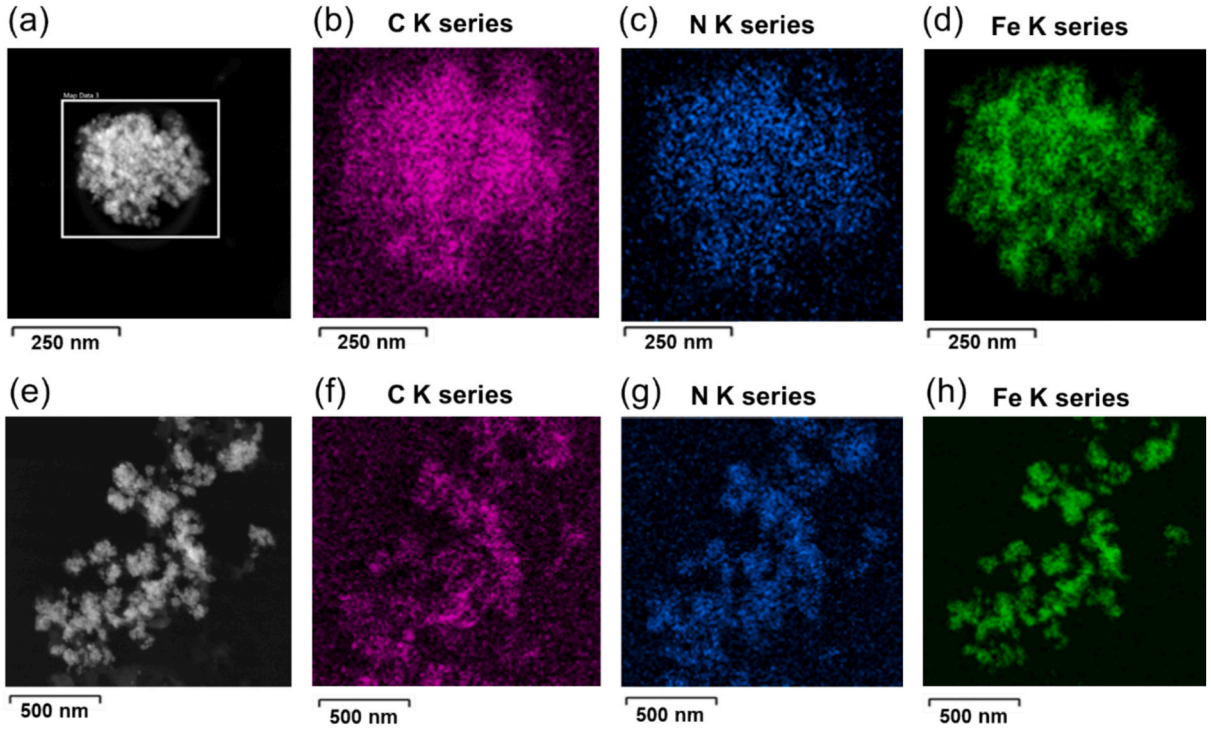

Fig. 4. TEM images of (a) Fc-Mel POP and (e) Fc-PBTD POP. EDS images of (b–d) Fc-Mel and (f–h) Fc-PBTD polymers.

probe interfacial charge-transfer resistance. Nyquist plots (Fig. 5d) reveal that Fc-PBTD POP@NF possesses a significantly lower charge-transfer resistance (R_{ct} = 125 Ω) than Fc-Mel POP@NF (R_{ct} = 244 Ω), confirming more efficient charge transport and improved electrical conductivity, which directly contribute to enhanced OER activity.

Long-term stability was evaluated via chronopotentiometry at a constant current density of 20 mA cm^{-2} over 15 h. Both catalysts exhibit stable potential profiles throughout the test, with Fc-PBTD POP@NF displaying the highest stability (Fig. 6a). Post-stability LSV measurements show negligible deviation from the initial polarization curve (Fig. 6b), confirming excellent structural and catalytic durability under prolonged OER conditions.

The electrochemically active surface area (ECSA) was estimated from the double-layer capacitance (C_{dl}) obtained from CV measurements at scan rates ranging from 25 to 150 mV s^{-1} (Fig. S13). The calculated C_{dl} values for pristine NF, Fc-Mel POP@NF, and Fc-PBTD POP@NF are 0.9, 1.3, and 1.85 mF cm^{-2}, respectively, indicating a significantly larger ECSA for Fc-PBTD POP@NF [67]. ECSA-normalized LSV curves (Fig. S14) show that Fc-PBTD POP@NF maintains superior activity at lower potentials, while Fc-Mel POP@NF exhibits higher currents only at higher overpotentials.

The Faradaic efficiency (FE) for oxygen evolution was determined by quantifying evolved O_2 using gas chromatography (GC-BID) and normalizing against the total charge passed. The Fc-PBTD POP@NF electrode exhibits a high FE of 96.2%, confirming efficient charge utilization for OER [68].

Structural stability after OER was further confirmed by XRD and XPS analyses. XRD patterns before and after OER show no new crystalline peaks or loss of amorphous features (Fig. S15a), indicating structural integrity of the polymer framework. XPS spectra reveal no new FeOx-related features or significant binding-energy shifts, confirming that Fe centers do not undergo irreversible oxidation (Fig. S15b) [52]. Importantly, Fe 2p spectra show an increased contribution from Fe(III) species after OER, consistent with reversible Fe(II)/Fe(III) redox cycling during catalysis. Together with the CV results, these observations support the role of Fc moieties as stable electron-transfer mediators rather than sacrificial species.

The superior OER performance of Fc-PBTD POP@NF can be attributed to its larger BET surface area (428 m^2 g^{-1} vs. 293 m^2 g^{-1} for Fc-Mel POP), higher ECSA, and more favorable microstructure, which together enhance OH^- adsorption, active-site exposure, and reaction kinetics. Beyond surface area effects, the intrinsic molecular structure of the PBTD linker plays a crucial role. Its extended π-conjugation improves charge delocalization and electron mobility, while alternating benzene and triazine units create a rigid, electronically modulated framework that stabilizes redox-active Fc centers and reaction intermediates. The bulkier and more linear PBTD linker also generates larger pore channels and a more open architecture, improving mass transport and active-site accessibility. Additionally, the higher nitrogen content enhances substrate binding and electronic interactions with OER intermediates. Collectively, these features account for the markedly enhanced OER activity and stability of Fc-PBTD POP@NF relative to Fc-Mel POP@NF [69–71].

The OER performance of the synthesized POP catalysts was evaluated in comparison with other reported polymeric electrocatalysts and commercially available noble metal catalysts, including IrO_2 and RuO_2, as detailed in Table S2. Among these, the Fc-PBTD catalyst stands out for its ability to achieve 10 mA cm^{-2} at lower overpotential, while also demonstrating the capacity to sustain a high current density of 340 mA cm^{-2}. These results highlight its exceptional catalytic efficiency and underscore its promise as a competitive alternative to conventional OER catalysts.

The excellent OER performance of Fc-PBTD POP is attributed to the synergistic interaction between its conjugated PBTD linker and Fc active centers. Under anodic polarization, Fc units can undergo reversible Fe (II)/Fe(III) oxidation, enhancing electron extraction from OH^- and facilitating OER intermediate formation. The electron-deficient triazine fragments within the PBTD linker further promote charge delocalization and stabilize high-valent Fe species. Literature reports suggest that ferrocene-based frameworks can partially reconstruct into FeOOH-like domains under OER conditions, which serve as the true catalytic centers [52]. It is plausible that Fc-PBTD POP undergoes a similar surface

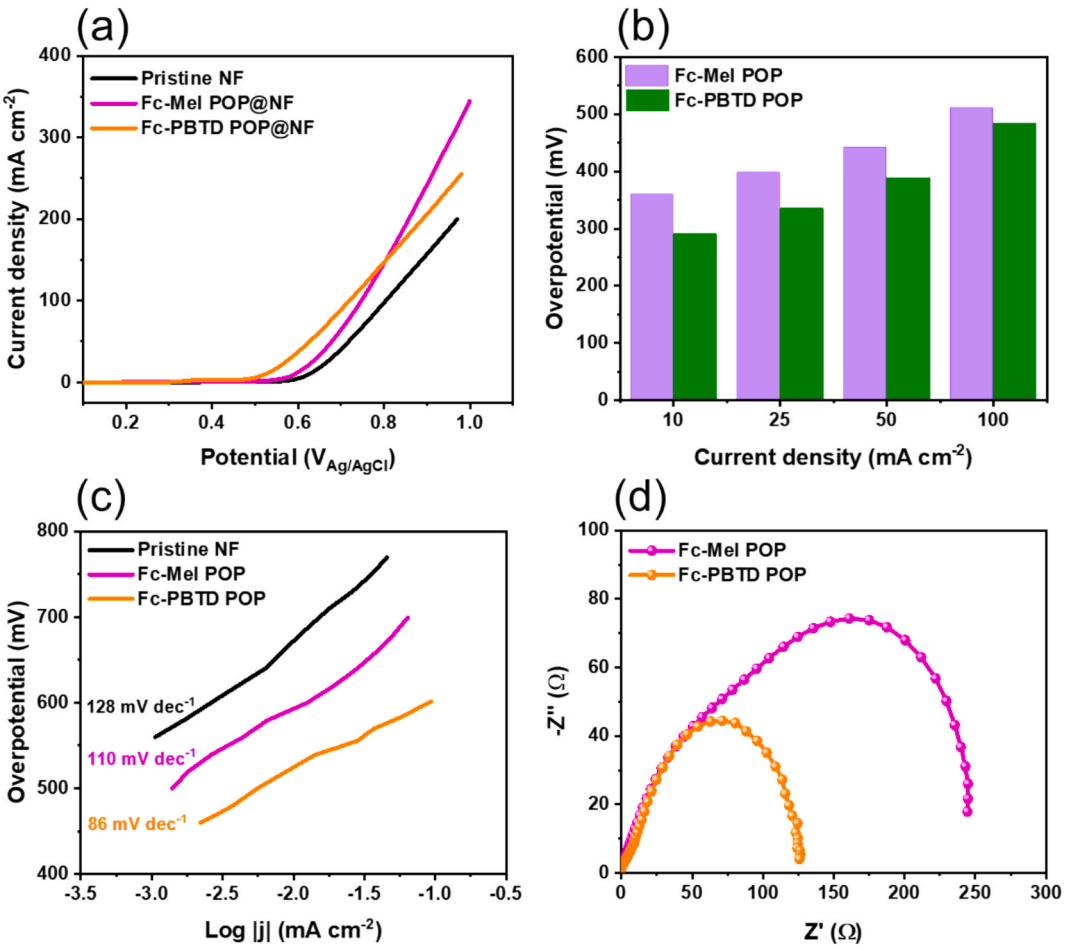

Fig. 5. Electrocatalytic OER studies: (a) LSV curves of different POP@NF electrocatalysts in 1.0 M KOH electrolyte solution. (b) Onset overpotential values for different as-developed electrodes. (c) Tafel plots and corresponding Tafel slope values for pristine NF and as-developed POP@NF catalysts. (d) EIS Nyquist plots for different POP electrocatalysts.

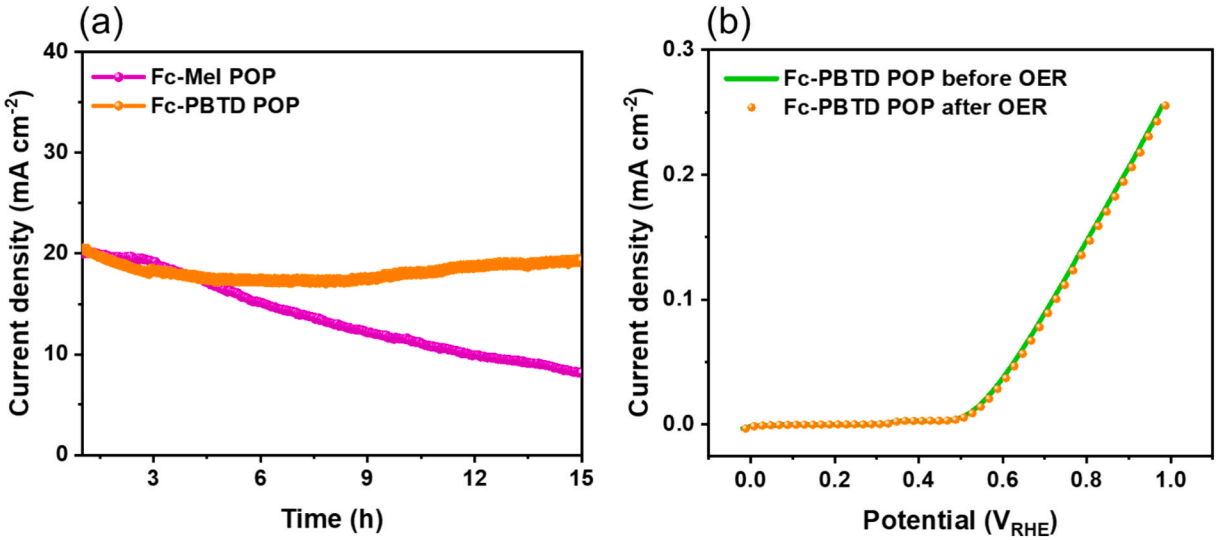

Fig. 6. Electrocatalytic OER investigations: (a) Chronopotentiometry long-term OER response of POP@NF catalysts. (b) LSV curves of the Fc-PBTD electrocatalyst before and after the chronopotentiometric study.

transformation, where the conjugated aromatic backbone maintains structural stability while the Fc moieties participate in forming Fe–OOH intermediates. Moreover, the extended π-conjugation of the PBTD unit improves charge mobility through the framework, resulting in faster electron transfer and lower overpotential. Collectively, these structural features rationalize the observed low overpotential, small Tafel slope,

and strong stability.

Raman spectroscopy provides additional mechanistic insight into the differing OER activities of the catalysts (Fig. S10). Fc-PBTD POP exhibits significantly stronger Raman bands in the 1000–1200 cm^{-1} region, which are assigned to aromatic C–C and C=N stretching vibrations, indicating a more rigid and highly π-conjugated framework compared with Fc-Mel POP. This enhanced conjugation is consistent with more efficient charge transport and improved stabilization of high-valent Fe–O intermediates during OER. Furthermore, more pronounced vibrational features in the low-frequency region (100–150 cm^{-1}), associated with Fc–Fe ring modes, are observed for Fc-PBTD POP, suggesting stronger electronic coupling between the Fc units and the polymer backbone. Collectively, these Raman features confirm that Fc-PBTD POP provides a more electronically delocalized and structurally robust catalytic platform, accounting for its lower overpotential and superior stability. Although post-OER or in situ Raman measurements would offer deeper insight into structural evolution under operating conditions, the present Raman analysis already provides compelling mechanistic evidence for the enhanced OER performance of Fc-PBTD POP.

4. Conclusion

In summary, two ferrocene-based porous organic polymer materials have been synthesized via a conventional solvothermal process involving a Schiff-base polymerization reaction. These POPs were supported on nickel foam as potential catalysts for the OER application. Among them, the Fc-PBTD POP@NF catalyst achieved 10 mA cm^{-2} current density at a lower overpotential of 291 mV with a smaller Tafel slope of 86 mV dec^{-1}, which is significantly better than the corresponding catalytic performance of the Fc-Mel POP@NF counterpart. Besides that, it showed OER stability up to 15 h without significant changes in electrochemical performance and a reduced charge transfer resistance of 125 Ω, which is significantly lower than that observed for the other catalyst examined in this study, indicating faster reaction kinetics and more efficient charge transport. The larger surface area and accessible morphology of the Fc-PBTD POP compared to the Fc-Mel POP electrocatalyst promote more active sites and facile electron transfer, and hence greater OER activity. Our study highlights one useful example for the development of efficient ferrocene-based POP materials as OER electrocatalysts.

CRediT authorship contribution statement

Ahmed F. Saber: Writing – original draft, Software, Methodology, Investigation, Formal analysis, Conceptualization. **Mohamed Gamal Mohamed:** Software, Methodology, Investigation, Formal analysis, Conceptualization. **Munzir H. Suliman:** Investigation, Formal analysis. **Shiao-Wei Kuo:** Writing – review & editing, Resources, Project administration, Funding acquisition. **Mahmoud M. Abdelnaby:** Writing – review & editing, Supervision, Resources, Project administration, Formal analysis.

Declaration of competing interest

The authors declare that they have no known competing financial interests or personal relationships that could have appeared to influence the work reported in this paper.

Acknowledgment

The authors acknowledge the Interdisciplinary Research Center for Hydrogen Technologies and Carbon Management (IRC-HTCM) at King Fahd University of Petroleum and Minerals (KFUPM) for its support.

Appendix A. Supplementary data

Supplementary data to this article can be found online at https://doi.org/10.1016/j.fuel.2026.138533.

Data availability

Data will be made available on request.

References

[1] Zhuo H, Chen W, Yang T, Wei C, Li W, Feng L, et al. Fe-doped N/S-rich carbon catalyst derived from porphyrine-ferrocene conjugated microporous polymer for bifunctional electrocatalysis and zinc-air batteries. Appl Catal A 2024;674:119617. https://doi.org/10.1016/J.APCATA.2024.119617.
[2] Yan W, Guo O, Xing Q, Liao M, Shi Z, Feng H, et al. Atomically Dispersed Ni–N4 Sites Assist Pt3Ni Nanocages with Pt Skin to Synergistically Enhance Oxygen Reduction activity and Stability. Small 2023;19:2300200. https://doi.org/10.1002/SMLL.202300200.
[3] Zhang Y, Yang J, Ge R, Zhang J, Cairney JM, Li Y, et al. The effect of coordination environment on the activity and selectivity of single-atom catalysts. Coord Chem Rev 2022;461:214493. https://doi.org/10.1016/J.CCR.2022.214493.
[4] Chu S, Majumdar A. Opportunities and challenges for a sustainable energy future. Nature 2012;488:294–303. https://doi.org/10.1038/NATURE11475;SUBJMETA.
[5] Chatenet M, Pollet BG, Dekel DR, Dekel F, Deseure J, Deseure P, et al. Water electrolysis: from textbook knowledge to the latest scientific strategies and industrial developments. Chem Soc Rev 2022;51:4583–762. https://doi.org/10.1039/D0CS01079K.
[6] Antolini E. Iridium As Catalyst and Cocatalyst for Oxygen Evolution/Reduction in Acidic Polymer Electrolyte Membrane Electrolyzers and fuel Cells. ACS Catal 2014;4:1426–40. https://doi.org/10.1021/CS4011875.
[7] Song F, Bai L, Moysiadou A, Lee S, Hu C, Liardet L, et al. Transition Metal Oxides as Electrocatalysts for the Oxygen Evolution Reaction in Alkaline Solutions: an Application-inspired Renaissance. J Am Chem Soc 2018;140:7748–59. https://doi.org/10.1021/JACS.8B04546.
[8] Raveendran A, Chandran M, Dhanusuraman R. A comprehensive review on the electrochemical parameters and recent material development of electrochemical water splitting electrocatalysts. RSC Adv 2023;13:3843–76. https://doi.org/10.1039/D2RA07642J.
[9] Wei C, Rao RR, Peng J, Huang B, Stephens IEL, Risch M, et al. Recommended Practices and Benchmark activity for Hydrogen and Oxygen Electrocatalysis in Water Splitting and fuel Cells. Adv Mater 2019;31:1806296. https://doi.org/10.1002/ADMA.201806296.
[10] Yin J, Li Y, Lv F, Lu M, Sun K, Wang W, et al. Oxygen vacancies Dominated NiS_2/CoS_2 Interface Porous Nanowires for Portable Zn–Air Batteries Driven Water Splitting Devices. Adv Mater 2017;29:1704681. https://doi.org/10.1002/ADMA.201704681.
[11] Reier T, Oezaslan M, Strasser P. Electrocatalytic Oxygen Evolution Reaction (OER) on Ru, Ir, and Pt Catalysts: a Comparative Study of Nanoparticles and Bulk Materials. ACS Catal 2012;2:1765–72. https://doi.org/10.1021/CS3003098.
[12] Cheng N, Stambula S, Wang D, Banis MN, Liu J, Riese A, et al. Platinum single-atom and cluster catalysis of the hydrogen evolution reaction. Nat Commun 2016;7:1–9. https://doi.org/10.1038/NCOMMS13638;TECHMETA.
[13] Du K, Zhang L, Shan J, Guo J, Mao J, Yang CC, et al. Interface engineering breaks both stability and activity limits of RuO2 for sustainable water oxidation. Nat Commun 2022;13:1–9. https://doi.org/10.1038/S41467-022-33150-X;TECHMETA.
[14] Staszak-Jirkovský J, Malliakas CD, Lopes PP, Danilovic N, Kota SS, Chang KC, et al. Design of active and stable Co-Mo-Sx chalcogels as pH-universal catalysts for the hydrogen evolution reaction. Nat Mater 2016;15:197–203. https://doi.org/10.1038/NMAT4481;SUBJMETA.
[15] Lee SW, Carlton C, Risch M, Surendranath Y, Chen S, Furutsuki S, et al. The Nature of Lithium Battery Materials under Oxygen Evolution Reaction Conditions. J Am Chem Soc 2012;134:16959–62. https://doi.org/10.1021/JA307814J.
[16] Feng M, Huang J, Peng Y, Huang C, Yue X, Huang S. Tuning Electronic Structures of transition Metal Carbides to boost Oxygen Evolution Reactions in Acidic Medium. ACS Nano 2022;16:13834–44. https://doi.org/10.1021/ACSNANO.2C02099.
[17] Li S, Chen B, Wang Y, Ye MY, van Aken PA, Cheng C, et al. Oxygen-evolving catalytic atoms on metal carbides. Nat Mater 2021;20:1240–7. https://doi.org/10.1038/S41563-021-01006-2;TECHMETA.
[18] Liu K, Zhang C, Sun Y, Zhang G, Shen X, Zou F, et al. High-Performance transition Metal Phosphide Alloy Catalyst for Oxygen Evolution Reaction. ACS Nano 2017;12:158–67. https://doi.org/10.1021/ACSNANO.7B04646.
[19] Tian J, Liu Q, Asiri AM, Sun X. Self-Supported Nanoporous Cobalt Phosphide Nanowire Arrays: an Efficient 3D Hydrogen-Evolving Cathode over the Wide Range of pH 0–14. J Am Chem Soc 2014;136:7587–90. https://doi.org/10.1021/JA503372R.
[20] Tareen AK, Priyanga GS, Khan K, Pervaiz E, Thomas T, Yang M. Nickel-based transition Metal Nitride Electrocatalysts for the Oxygen Evolution Reaction. ChemSusChem 2019;12:3941–54. https://doi.org/10.1002/CSSC.201900553.
[21] Zhai P, Wang C, Zhao Y, Zhang Y, Gao J, Sun L, et al. Regulating electronic states of nitride/hydroxide to accelerate kinetics for oxygen evolution at large current

density. Nat Commun 2023;14:1–11. https://doi.org/10.1038/S41467-023-37091-X;TECHMETA.
[22] Shi Y, Du W, Zhou W, Wang C, Lu S, Lu S, et al. Unveiling the Promotion of Surface-Adsorbed Chalcogenate on the Electrocatalytic Oxygen Evolution Reaction. Angew Chem Int Ed 2020;59:22470–4. https://doi.org/10.1002/ANIE.202011097.
[23] Jaramillo TF, Jørgensen KP, Bonde J, Nielsen JH, Horch S, Chorkendorff I. Identification of active Edge Sites for Electrochemical H_2 Evolution from MoS_2 Nanocatalysts. Science 2007;317:100–2. https://doi.org/10.1126/SCIENCE.1141483.
[24] Liu X, Dai L. Carbon-based metal-free catalysts Nat Rev Mater 2016;1:1–12. https://doi.org/10.1038/natrevmats.2016.64.
[25] Yuan S, Peng J, Cai B, Huang Z, Garcia-Esparza AT, Sokaras D, et al. Tunable metal hydroxide–organic frameworks for catalysing oxygen evolution. Nat Mater 2022;21:673–80. https://doi.org/10.1038/S41563-022-01199-0.
[26] Liu W, Ni C, Gao M, Zhao X, Zhang W, Li R, et al. Metal–Organic-Framework-based Nanoarrays for Oxygen Evolution Electrocatalysis. ACS Nano 2023;17:24564–92. https://doi.org/10.1021/ACSNANO.3C09261.
[27] Zhang L, Xu Q, Xia L, Jiang W, Wang K, Cao P, et al. Asymmetrically tailored catalysts towards electrochemical energy conversion with non-precious materials. Chem Soc Rev 2025;54:5108–45. https://doi.org/10.1039/D4CS00710G.
[28] Li HJW, Lin Y, Duan J, Wen Q, Liu Y, Zhai T. Stability of electrocatalytic OER: from principle to application. Chem Soc Rev 2024;53:10709–40. https://doi.org/10.1039/D3CS00010A.
[29] Zhang T, Gregoriou VG, Gasparini N, Chochos CL. Porous organic polymers in solar cells. Chem Soc Rev 2022;51:4465–83. https://doi.org/10.1039/D2CS00123C.
[30] Tian L, Zhou S, Zhao J, Xu Q, Li N, Chen D, et al. Sulfonate-modified calixarene-based porous organic polymers for electrostatic enhancement and efficient rapid removal of cationic dyes in water. J Hazard Mater 2023;441:129873. https://doi.org/10.1016/J.JHAZMAT.2022.129873.
[31] Saber AF, Elewa AM, Chou HH, EL-Mahdy AFM. Donor to Acceptor Charge transfer in Carbazole-based Conjugated Microporous Polymers for Enhanced Visible-Light-Driven Photocatalytic Water Splitting. ChemCatChem 2023;15:e202201287. https://doi.org/10.1002/CCTC.202201287.
[32] Saber AF, Chueh CC, Rashad M, Kuo SW, EL-Mahdy AFM. Thiazolyl-linked conjugated microporous polymers for enhancement adsorption and photocatalytic degradation of organic dyes from water. Mater Today Sustain 2023;23:100429. https://doi.org/10.1016/J.MTSUST.2023.100429.
[33] Sun H, Awada H, Lei H, Aljabour A, Song L, Offenthaler S, et al. Tuning ORR selectivity of π-conjugated cobalt corroles from $2e^-$ to $4e^-$. Mater Today Catal 2024;4:100038. https://doi.org/10.1016/J.MTCATA.2023.100038.
[34] Saber AF, Kuo SW, EL-Mahdy AFM. Microporous carbons derived from nitrogen-rich triazatruxene-based porous organic polymers for efficient cathodic supercapacitors. J Mater Chem A 2024;12:15373–85. https://doi.org/10.1039/D4TA01242A.
[35] Saber AF, Ahmed M, Kuo SW, EL-Mahdy AFM. Tetraphenylcyclopentadiene-based conjugated microporous polymers for high-performance energy storage carbons. Polym Chem 2023;14:4079–88. https://doi.org/10.1039/D3PY00671A.
[36] Yang DH, Tao Y, Ding X, Han BH. Porous organic polymers for electrocatalysis. Chem Soc Rev 2022;51:761–91. https://doi.org/10.1039/D1CS00887K.
[37] Saber AF, Abdelnaser S, EL-Mahdy AFM, Kuo SW. One-pot synthesis of heteroatom-rich anthraquinone-based benzoxazine-linked porous organic polymers for high performance supercapacitors. Electrochim Acta 2025;511:145397. https://doi.org/10.1016/J.ELECTACTA.2024.145397.
[38] Saber AF, EL-Mahdy AFM, Kuo SW. Development of heteroatom-rich fluorene-based benzoxazine-linked porous organic polymers as potential candidates for energy storage. J Taiwan Inst Chem Eng 2025;168:105935. Doi: 10.1016/J.JTICE.2024.105935.
[39] Saber AF, Liao HT, Li PJ, Chen YF, Mabuti L, Kuo SW, et al. Synergistic structural engineering of donor–acceptor–acceptor type conjugated microporous polymers as photocatalysts for boosting sunlight-driven hydrogen evolution. J Colloid Interface Sci 2025;699:138156. https://doi.org/10.1016/J.JCIS.2025.138156.
[40] Zhu HJ, Si DH, Guo H, Chen Z, Cao R, Huang YB. Oxygen-tolerant CO_2 electroreduction over covalent organic frameworks via photoswitching control oxygen passivation strategy. Nat Commun 2024;15:1–11. https://doi.org/10.1038/S41467-024-45959-9.
[41] Guo H, Si DH, Zhu HJ, Chen ZA, Cao R, Huang YB. Boosting CO_2 Electroreduction over a Covalent Organic Framework in the Presence of Oxygen. Angew Chem Int Ed 2024;63:e202319472. https://doi.org/10.1002/ANIE.202319472.
[42] Wu QJ, Si DH, Wu Q, Dong YL, Cao R, Huang YB. Boosting Electroreduction of CO_2 over Cationic Covalent Organic Frameworks: Hydrogen Bonding Effects of Halogen Ions. Angew Chem Int Ed 2023;62:e202215687. https://doi.org/10.1002/ANIE.202215687.
[43] Zhao X, Yin Q, Mao X, Cheng C, Zhang L, Wang L, et al. Theory-guided design of hydrogen-bonded cobaltoporphyrin frameworks for highly selective electrochemical H_2O_2 production in acid. Nat Commun 2022;13:1–8. https://doi.org/10.1038/S41467-022-30523-0.
[44] Ding J, Guan X, Lv J, Chen X, Zhang Y, Li H, et al. Three-Dimensional Covalent Organic Frameworks with Ultra-Large Pores for Highly Efficient Photocatalysis. J Am Chem Soc 2023;145:3248–54. https://doi.org/10.1021/JACS.2C13817.
[45] Tang J, Liang Z, Qin H, Liu X, Zhai B, Su Z, et al. Large-area Free-standing Metalloporphyrin-based Covalent Organic Framework Films by Liquid-air Interfacial Polymerization for Oxygen Electrocatalysis. Angew Chem Int Ed 2023;135:e202214449. https://doi.org/10.1002/ANGE.202214449.
[46] Tan L, Tan B. Hypercrosslinked porous polymer materials: design, synthesis, and applications. Chem Soc Rev 2017;46:3322–56. https://doi.org/10.1039/C6CS00851H.
[47] Xie Z, Li YS, Chen L, Jiang D. Functional conjugated porous polymer materials. Acta Polym Sin 2016;12:1621–34. https://doi.org/10.11777/j.issn1000-3304.2016.16222.
[48] Yang C, Yang ZD, Dong H, Sun N, Lu Y, Zhang FM, et al. Theory-Driven Design and Targeting Synthesis of a Highly-Conjugated Basal-Plane 2D Covalent Organic Framework for Metal-Free Electrocatalytic OER. ACS Energy Lett 2019;4:2251–8. https://doi.org/10.1021/ACSENERGYLETT.9B01691.
[49] Mondal S, Mohanty B, Nurhuda M, Dalapati S, Jana R, Addicoat M, et al. A Thiadiazole-based Covalent Organic Framework: a Metal-Free Electrocatalyst toward Oxygen Evolution Reaction. ACS Catal 2020;10:5623–30. https://doi.org/10.1021/ACSCATAL.9B05470.
[50] Das SK, Shyamal S, Das M, Mondal S, Chowdhury A, Chakraborty D, et al. Metal-Free Pyrene-based Conjugated Microporous Polymer Catalyst Bearing N- and S-Sites for Photoelectrochemical Oxygen Evolution Reaction. Front Chem 2021;9:803860. https://doi.org/10.3389/FCHEM.2021.803860.
[51] Li H, Pan F, Qin C, Wang T, Chen KJ. Porous Organic Polymers-based Single-Atom Catalysts for Sustainable Energy-Related Electrocatalysis. Adv Energy Mater 2023;13:2301378. https://doi.org/10.1002/AENM.202301378.
[52] Doughty T, Zingl A, Wünschek M, Pichler CM, Watkins MB, Roy S. Structural Reconstruction of a Cobalt- and Ferrocene-based Metal–Organic Framework during the Electrochemical Oxygen Evolution Reaction. ACS Appl Mater Interfaces 2024;16:40814–24. https://doi.org/10.1021/ACSAMI.4C03262.
[53] Li S, Shangguan X, Zhou Z, Niu W, Zhang Y, Wang X, et al. Immobilization of ferrocene and its derivatives within metal–organic frameworks with high loadings toward efficient oxygen evolution reaction. Dalton Trans 2024;53:1568–74. https://doi.org/10.1039/D3DT02763E.
[54] Khrizanforova V, Shekurov R, Miluykov V, Khrizanforov M, Bon V, Kaskel S, et al. 3D Ni and Co redox-active metal–organic frameworks based on ferrocenyl diphosphinate and 4,4′-bipyridine ligands as efficient electrocatalysts for the hydrogen evolution reaction. Dalton Trans 2020;49:2794–802. https://doi.org/10.1039/C9DT04834K.
[55] Liang J, Gao X, Guo B, Ding Y, Yan J, Guo Z, et al. Ferrocene-based Metal–Organic Framework Nanosheets as a Robust Oxygen Evolution Catalyst. Angew Chem Int Ed 2021;60:12770–4. https://doi.org/10.1002/ANIE.202101878.
[56] Zhou B, Liu L, Cai P, Zeng G, Li X, Wen Z, et al. Ferrocene-based porous organic polymer derived high-performance electrocatalysts for oxygen reduction. J Mater Chem A 2017;5:22163–9. https://doi.org/10.1039/C7TA06515A.
[57] Saber AF, EL-Mahdy AFM. (E)-1,2-Diphenylethene-based conjugated nanoporous polymers for a superior adsorptive removal of dyes from water. New J Chem 2021;45:21834–21843. Doi: 10.1039/D1NJ04287D.
[58] Saber AF, Suliman MH, Tayeb AM, Essalhi M, Elsayed MH, Sabbah A, et al. Engineering of Copper-based Nitrogen-Rich Covalent Triazine Frameworks (Cu@CTFs) as Highly Efficient Electrocatalysts for Carbon Dioxide Reduction. Chem Asian J 2025;20:e70292. https://doi.org/10.1002/asia.70292.
[59] Saber AF, Chen YF, Mabuti L, Chaganti SV, Sharma SU, Lüder J, et al. Engineering carbonyl-rich conjugated microporous polymers with a pyrene-4,5,9,10-tetraone building block as highly efficient and stable electrodes for energy storage. Mater Adv 2025;6:607–16. https://doi.org/10.1039/D4MA00928B.
[60] Ehsan MA, Khan A, Zafar MN, Akber UA, Hakeem AS, Nazar MF. Aerosol-assisted chemical vapor deposition of nickel sulfide nanowires for electrochemical water oxidation. Int J Hydrogen Energy 2022;47:42001–12. https://doi.org/10.1016/J.IJHYDENE.2021.10.231.
[61] Babar NUA, Hakeem AS, Ehsan MA. Direct Fabrication of Nanoscale NiVOx Electrocatalysts over Nickel Foam for a High-Performance Oxygen Evolution Reaction. ACS Appl Energy Mater 2022;5:4318–28. https://doi.org/10.1021/ACSAEM.1C03940.
[62] Torriero AAJ, Mruthunjaya AKV. Ferrocene-Based Electrochemical Sensors for Cations Inorganics 2023;11:472. https://doi.org/10.3390/INORGANICS11120472.
[63] Fabbrizzi L. The ferrocenium/ferrocene couple: a versatile redox switch. ChemTexts 2020;6:22. https://doi.org/10.1007/S40828-020-00119-6/FIGURES/26.
[64] Fontanesi C, Como ED, Vanossi D, Montecchi M, Cannio M, Mondal PC, et al. Redox-active Ferrocene grafted on H-Terminated Si(111): Electrochemical Characterization of the Charge Transport Mechanism and Dynamics. Sci Rep 2019;9:8735. https://doi.org/10.1038/s41598-019-45448-w.
[65] McCrory CCL, Jung S, Peters JC, Jaramillo TF. Benchmarking Heterogeneous Electrocatalysts for the Oxygen Evolution Reaction. J Am Chem Soc 2013;135:16977–87. https://doi.org/10.1021/JA407115P.
[66] Meng J, Xu Z, Li H, Young DJ, Hu C, Yang Y. Porphyrin-based NiFe Porous Organic Polymer Catalysts for the Oxygen Evolution Reaction. ChemCatChem 2021;13:1396–402. https://doi.org/10.1002/CCTC.202001876.
[67] Liu Y, Zhang L, Xu Q, Zhang S, Zhou Y, Hu G. Oxophilic Low-Coordination Gd-N3 Single Atom Sites with P-Enhanced Second Coordination for High-Performance Al-Air Batteries. Adv Funct Mater 2025;35:2413134. https://doi.org/10.1002/adfm.202413134.
[68] Xu Q, Zhang L, Li L, Zhang S, Zhou Y, Hu G. Harnessing Multi-Asymmetric Engineering: a New Horizon in Bifunctional Oxygen Electrocatalysis with Iron-Group Atom-Cluster Nanohybrid. Adv Funct Mater 2025;35:2414379. https://doi.org/10.1002/adfm.202414379.

[69] Cui X, Wu M, Liu X, He B, Zhu Y, Jiang Y, et al. Engineering organic polymers as emerging sustainable materials for powerful electrocatalysts. Chem Soc Rev 2024; 53:1447–94. https://doi.org/10.1039/D3CS00727H.
[70] Dou Y, Wang A, Zhao L, Yang X, Wang Q, Sudi MS, et al. Boosted hydrogen evolution reaction for a nitrogen-rich azo-bridged metallated porphyrin network. J Colloid Interface Sci 2023;650:943–50. https://doi.org/10.1016/J.JCIS.2023.07.051.
[71] Xu Y, Jin S, Xu H, Nagai A, Jiang D. Conjugated microporous polymers: design, synthesis and application. Chem Soc Rev 2013;42:8012–31. https://doi.org/10.1039/C3CS60160A.